



## Promotional role of BaCO<sub>3</sub> on the chromium-tolerance of La<sub>0.6</sub>Sr<sub>0.4</sub>Co<sub>0.2</sub>Fe<sub>0.8</sub>O<sub>3-δ</sub> cathodes of solid oxide fuel cells

Jiongyuan Huang<sup>a</sup>, Quan Liu<sup>a</sup>, San Ping Jiang<sup>b,c</sup>, Ling Zhao<sup>d</sup>, Na Ai<sup>e</sup>, Xin Wang<sup>a</sup>, Yanqun Shao<sup>a</sup>, Chengzhi Guan<sup>f,\*</sup>, Huihuang Fang<sup>g</sup>, Yu Luo<sup>g</sup>, Kongfa Chen<sup>a,\*</sup>

<sup>a</sup> College of Materials Science and Engineering, Fuzhou University, Fuzhou, Fujian 350108, China

<sup>b</sup> Foshan Xianhu Laboratory of the Advanced Energy Science and Technology Guangdong Laboratory, Foshan 528216, China

<sup>c</sup> WA School of Mines: Minerals, Energy and Chemical Engineering, Curtin University, Perth, WA 6102, Australia

<sup>d</sup> Faculty of Materials Science and Chemistry, China University of Geosciences, Wuhan 430074, China

<sup>e</sup> Fujian College Association Instrumental Analysis Center, Fuzhou University, Fuzhou, Fujian 350108, China

<sup>f</sup> Key Laboratory of Interfacial Physics and Technology, Shanghai Institute of Applied Physics, Chinese Academy of Sciences, Shanghai 201800, China

<sup>g</sup> National Engineering Research Center of Chemical Fertilizer Catalyst (NERC-CFC), College of Chemical Engineering, Fuzhou University, Fuzhou, Fujian 350002, China



### ARTICLE INFO

#### Keywords:

Solid oxide fuel cells  
BaCO<sub>3</sub> infiltration  
Chromium-tolerance  
Barium chromate

### ABSTRACT

Degradation of cathodes caused by the gaseous Cr species from a Fe–Cr alloy interconnect is a key issue in the development of durable solid oxide fuel cells technologies. Herein, we explore the effect of infiltration of BaCO<sub>3</sub> nanoparticles on the electrocatalytic performance and Cr-tolerance of La<sub>0.6</sub>Sr<sub>0.4</sub>Co<sub>0.2</sub>Fe<sub>0.8</sub>O<sub>3-δ</sub> (LSCF) cathodes. The BaCO<sub>3</sub> increases the performance of LSCF and the single-cell delivers a peak power density of 1.30 W cm<sup>-2</sup> at 800 °C. The BaCO<sub>3</sub> gives rise to no Cr deposition and Sr segregation on LSCF after exposure in gaseous CrO<sub>3</sub>, while a BaCrO<sub>4</sub> surface layer is deposited on the cathode in contact with a Fe–Cr alloy. The synergistic effects of BaCrO<sub>4</sub> layer on mitigating the reaction between segregated Sr and Cr<sub>2</sub>O<sub>3</sub> and the very slow kinetics of reaction between BaCO<sub>3</sub> and CrO<sub>3</sub> contribute to the exceptional Cr-tolerance of the BaCO<sub>3</sub> infiltrated LSCF cathodes.

### 1. Introduction

In recent years, people have broadened horizons to innovative power generation devices for potentially solving the problems of energy shortage and excessive carbon emissions. Solid oxide fuel cells (SOFCs) are environmentally friendly energy conversion devices that possess many advantages including high energy conversion efficiency, low environmental pollution, and wide fuel adaptability. With the effective reduction of operating temperatures of SOFCs from traditional 1000 °C to intermediate temperatures of 600–800 °C (IT-SOFCs), metals such as Fe–Cr stainless steel alloy are commonly used as an interconnect material ascribed to their acceptable oxidation resistance, high electrical conductivity, and low price [1]. However, under the operating conditions of SOFCs, gaseous Cr species such as CrO<sub>3</sub> and CrO<sub>2</sub>(OH)<sub>2</sub> are generated from the Cr<sub>2</sub>O<sub>3</sub> scale layer that is thermally grown on the Fe–Cr alloy interconnect, leading to the Cr deposition and poisoning of the cathodes [2–6]. It is well accepted that Cr poisoning is one of the most significant degradation mechanisms of SOFCs technologies.

La<sub>0.6</sub>Sr<sub>0.4</sub>Co<sub>0.2</sub>Fe<sub>0.8</sub>O<sub>3-δ</sub> (LSCF) is one of the most representative

mixed ion/electron conducting cathodes for IT-SOFCs with high surface exchange and fast ion transport ability for oxygen reduction reaction (ORR) [7,8]. However, LSCF suffers from segregation of Sr cations on the surface [9–13], and the segregated Sr cations tend to act as a nucleation agent for Sr–Cr–O nuclei upon exposure in a gaseous Cr environment, initializing the formation of an insulating SrCrO<sub>4</sub> and Cr<sub>2</sub>O<sub>3</sub> surface layer [14,15]. Additionally, the resultant A-site Sr deficiency substantially reduces the electrocatalytic activity and stability of LSCF cathodes [16–18]. The fabrication of a protective layer on the Fe–Cr interconnect significantly mitigates the Cr volatility, however, it is almost impossible to completely eliminate the Cr deposition on the cathodes [19,20]. It is thus intrinsically essential to enhance the Cr-tolerance of the LSCF cathodes.

Much work has been carried out to develop Cr-tolerant cathodes [21–29]. Among these cathodes, Ba cations are extensively present either in the lattice of cathodes such as La<sub>0.6</sub>Sr<sub>0.4-x</sub>Ba<sub>x</sub>Co<sub>0.2</sub>Fe<sub>0.8</sub>O<sub>3-δ</sub> (LSBCF), La<sub>0.24</sub>Sr<sub>0.16</sub>Ba<sub>0.6</sub>Co<sub>0.5</sub>Fe<sub>0.44</sub>Nb<sub>0.06</sub>O<sub>3-δ</sub> (LSBCFN), Ba<sub>0.9</sub>Co<sub>0.7</sub>Fe<sub>0.2</sub>Nb<sub>0.1</sub>O<sub>3</sub> (BCFN), and La<sub>0.2</sub>Sr<sub>0.2</sub>Pr<sub>0.2</sub>Y<sub>0.2</sub>Ba<sub>0.2</sub>Co<sub>0.2</sub>Fe<sub>0.8</sub>O<sub>3-δ</sub> [30–37], or in a secondary phase used to decorate the LSCF cathodes

\* Corresponding authors.

E-mail addresses: [guanchengzhi@sinap.ac.cn](mailto:guanchengzhi@sinap.ac.cn) (C. Guan), [kongfa.chen@fzu.edu.cn](mailto:kongfa.chen@fzu.edu.cn) (K. Chen).

[38–41]. Our preliminary work has shown that the incorporation of BaCO<sub>3</sub> nanoparticles remarkably suppresses the Cr poisoning effect on the LSCF cathodes by forming a conducting BaCrO<sub>4</sub> surface layer rather than the insulating SrCrO<sub>4</sub> layer [42]. The blocking effect of forming a BaCrO<sub>4</sub> layer on the Cr deposition and poisoning is also reported on the Ba<sub>0.5</sub>Sr<sub>0.5</sub>Co<sub>0.8</sub>Fe<sub>0.2</sub>O<sub>3-δ</sub> (BSCF) and LSBCF cathodes [43,44]. Niu et al. applied a mixed BCFN and BaCO<sub>3</sub> coating into the LSCF cathode to improve the electrode performance and Cr poisoning resistance, and they pointed out that the thermodynamic inertness between BaCO<sub>3</sub> and gaseous CrO<sub>3</sub> or Cr(HO<sub>2</sub>)<sub>2</sub> contributed to the Cr-tolerance of LSCF [40]. Therefore, it has been experimentally proven that the Ba cations play a key role in suppressing the Cr poisoning effect, although there are great discrepancies in understanding the promotional role.

Here, we attempt to explore the promotional role of infiltration of BaCO<sub>3</sub> on the Cr-tolerance of LSCF. The incorporation of extrinsic BaCO<sub>3</sub> as the source of Ba is beneficial to avoid the potential negative effect of loss of lattice Ba on the structural stability of Ba doped cathodes, and the low loading of BaCO<sub>3</sub> makes it practically viable for massive application. The present results show that the incorporation of a small amount of BaCO<sub>3</sub> nanoparticles not only eliminates the Cr deposition and Sr segregation on the surface of LSCF bar sample in a gaseous CrO<sub>3</sub> environment, but also significantly mitigates the Sr segregation on the LSCF cathode under accelerated Cr poisoning conditions, and therefore, the promotional role of infiltration of BaCO<sub>3</sub> is proposed.

## 2. Experimental

### 2.1. Fabrication of anode-supported single-cells and half-cells

Anode-supported single-cells with a configuration of NiO-yttria-stabilized zirconia (YSZ) anode substrate/NiO-YSZ anode functional layer (AFL)/YSZ electrolyte layer/Gd<sub>0.1</sub>Ce<sub>0.9</sub>O<sub>1.95</sub> (GDC) buffer layer were fabricated by the procedures as described elsewhere [45,46]. The supported YSZ films were co-fired at 1450 °C for 5 h, while the GDC buffer layer was sintered at 1150 °C for 2 h. La<sub>0.6</sub>Sr<sub>0.4</sub>Co<sub>0.2</sub>Fe<sub>0.8</sub>O<sub>3-δ</sub> (LSCF, Fuel Cell Materials) cathode ink was prepared by combining LSCF powder with an ink vehicle (ethyl cellulose and terpineol of 4: 96 in mass ratio) in a mass ratio of 6:4. The cathode ink was screen-printed on the GDC layer and sintered at 1000 °C for 2 h. The area of the cathode was 0.22 cm<sup>2</sup>. The microstructure of the fractured button cells is shown in Fig. S1.

Half-cells with GDC electrolyte pellets were fabricated. The pellets were prepared by uniaxially compacting GDC powder (AGC Seimi Chemical Co Ltd.) and firing at 1450 °C for 5 h. The LSCF cathode ink was screen-printed on one side of the GDC pellets with an area of 0.5 cm<sup>2</sup> and sintered at 1000 °C for 2 h. The Pt ink (Gwent Electronic Materials Ltd) was screen-printed on the opposite side of GDC pellets as counter and reference electrodes.

Ba(NO<sub>3</sub>)<sub>2</sub> aqueous solution of 0.15 M was prepared by dissolving Ba(NO<sub>3</sub>)<sub>2</sub> (99.5 %) in deionized water. Citric acid (99.5 %) was added as a surfactant and complexing agent, and the molar ratio of Ba ions and citric acid was 1: 1. The Ba(NO<sub>3</sub>)<sub>2</sub> solution was infiltrated into the LSCF cathodes by a micro pipette, dried at room temperature, and fired at 700 °C for 2 h. The area specific loading of BaCO<sub>3</sub> was 0.46 mg cm<sup>-2</sup>, equal to a mass ratio of 3 wt% of the whole infiltrated cathodes. The BaCO<sub>3</sub> infiltrated LSCF cathode was denoted as BaCO<sub>3</sub>-LSCF cathode. The fabrication procedures of single-cells and half-cells are illustrated in Fig. S2.

### 2.2. Testing of single-cells and half-cells

A commercial sealant (Ceramabond 552-VFG, Aremco) was used to seal the button cell. Humidified H<sub>2</sub> with 3 % H<sub>2</sub>O was supplied to the anode at a flow rate of 50 ml min<sup>-1</sup>, and the cathode was exposed to ambient air. Discharge curves and impedance spectra were obtained by Gamry Interface 1000E in a temperature range of 600–800 °C. The

impedance spectra were measured at a cell voltage of 1 V, so as to make them more comparable between different single-cells [47]. The impedance spectra were analyzed using the distribution of relaxation time (DRT) [48,49]. The operating stability of the BaCO<sub>3</sub>-LSCF cell was monitored at 0.2 A cm<sup>-2</sup> and 800 °C by Arbin MITS Pro 4.0-BT 2000.

The Cr-tolerance of LSCF and BaCO<sub>3</sub>-LSCF cathodes was investigated using half-cells at 800 °C. A bare Fe-Cr alloy interconnect (RA446, 23–27 % Cr, Rolled Alloy Co) with no protective coating was placed on the surface of cathodes as the current collector and source of chromium to accelerate the Cr deposition and poisoning [3,50]. The cathodes were in contact with the ribs of interconnect where the interaction between Cr<sub>2</sub>O<sub>3</sub> and cathodes occurs via solid-state diffusion. Dry air (100 ml min<sup>-1</sup>) was flowed to the cathodes and counter electrodes. The galvanostatic stability of the half-cells were monitored at 0.2 A cm<sup>-2</sup>. The impedance spectra were measured at open-circuit, in frequencies of 0.1 Hz–100 kHz with a 10 mV AC signal.

### 2.3. Fabrication and electrical conductivity relaxation measurement of bar samples

To evaluate the variation of surface exchange ability in a gaseous CrO<sub>3</sub> environment, the electrical conductivity relaxation (ECR) curves of dense LSCF and BaCO<sub>3</sub>-LSCF rectangular bar samples were measured. To obtain LSCF bar samples, LSCF powder was pelletized at 200 MPa and sintered at 1300 °C for 5 h. The as-sintered bars were in the size of 25 mm × 6.50 mm × 0.54 mm. The 0.15 M Ba(NO<sub>3</sub>)<sub>2</sub> solution was dispersed on the surface of LSCF bar samples and heat-treated at 700 °C for 2 h to form the BaCO<sub>3</sub>-LSCF bar samples. The bar samples and an alumina crucible with Cr<sub>2</sub>O<sub>3</sub> powder were placed together in a quartz tube furnace at 800 °C without direct contact, and the atmosphere was dry synthetic air (N<sub>2</sub> + O<sub>2</sub> mixture with an oxygen partial pressure of 0.21 bar) at a flow rate of 100 ml min<sup>-1</sup> and an atmospheric pressure. The partial pressure of gaseous CrO<sub>3</sub> on the surface of bar samples is estimated in the range of 10<sup>-10</sup>–10<sup>-9</sup> atm [51]. The ECR measurement of the bar samples was performed with a four-probe method by a Keithley 2000 digital multimeter connected with a computer. The measurements were carried out at 800 °C in 50 ml min<sup>-1</sup> N<sub>2</sub> + O<sub>2</sub> mixture with an oxygen partial pressure varied from 0.05 bar to 0.21 bar. The ECR measurements were conducted as a function of exposure time in the gaseous CrO<sub>3</sub> environment. The oxygen surface exchange coefficients were calculated by fitting the ECR curves using the theoretical equation [52].

### 2.4. Microstructure and phase characterizations

The crystallographic phases of as-prepared and post-mortem LSCF and BaCO<sub>3</sub>-LSCF cathodes before and after the tests in the contact with the Fe-Cr interconnect were recognized by X-ray diffraction (XRD, Bruker D8 Advance) and a Laser Micro Raman Spectrometer (Renishaw Invia Reflex). The microstructure and elemental analysis of LSCF and BaCO<sub>3</sub>-LSCF cathodes and bar samples before and after the Cr-poisoning tests were performed using a scanning electron microscope (SEM, Zeiss Neon 40EsB) together with an X-ray energy dispersive spectroscope (EDS). The topography and morphology of the bar samples were also characterized by a Dimension FastScan atomic force microscope (AFM, Bruker). The 0.46 mg cm<sup>-2</sup> BaCO<sub>3</sub>-LSCF powder was scraped from an as-prepared cathode on the GDC electrolyte, and the morphology was examined by a high angle annular dark field scanning transmission electron microscope (HAADF-STEM, FEI Tecnai G2F20). X-ray photoelectron spectroscopy (XPS) core levels were carried out on the as-prepared LSCF and BaCO<sub>3</sub>-LSCF cathodes and the post-mortem LSCF and BaCO<sub>3</sub>-LSCF bar samples after the Cr poisoning tests, using a Kratos AXIS Ultra DLD system.

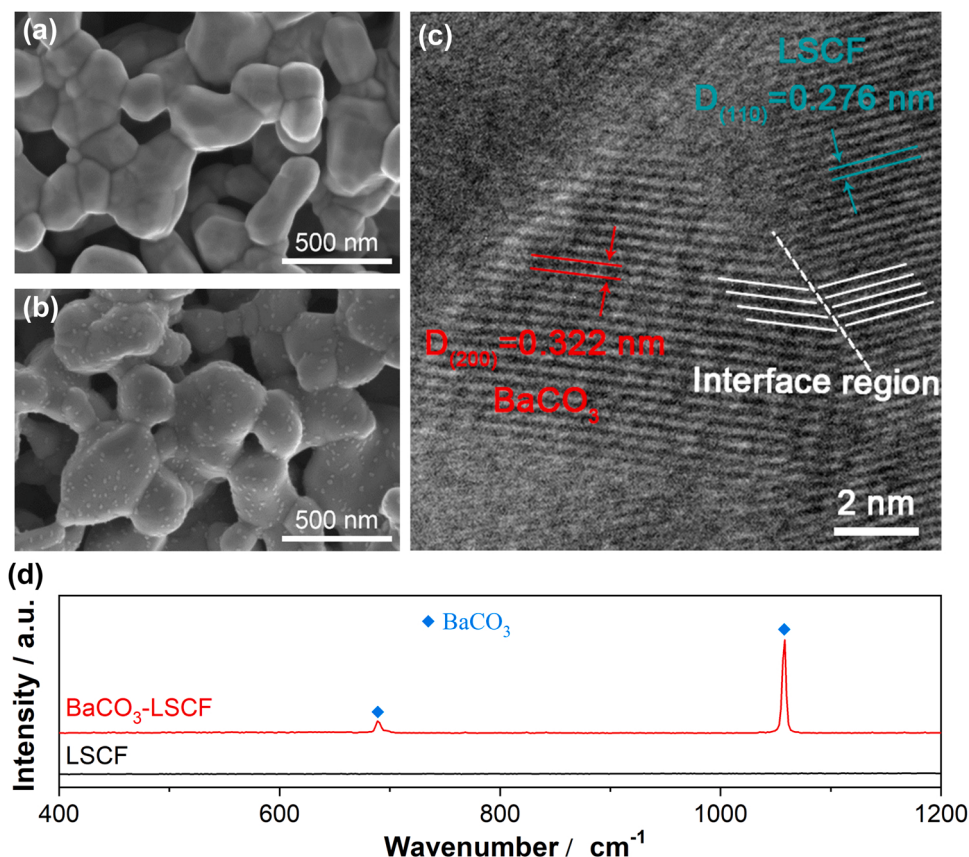


**Fig. 1.** SEM images of surface of as prepared (a) LSCF and (b) BaCO<sub>3</sub>-LSCF electrodes. (c) HRTEM image of BaCO<sub>3</sub>-LSCF powder. (d) Raman spectra obtained on the surface of LSCF and BaCO<sub>3</sub>-LSCF electrodes.

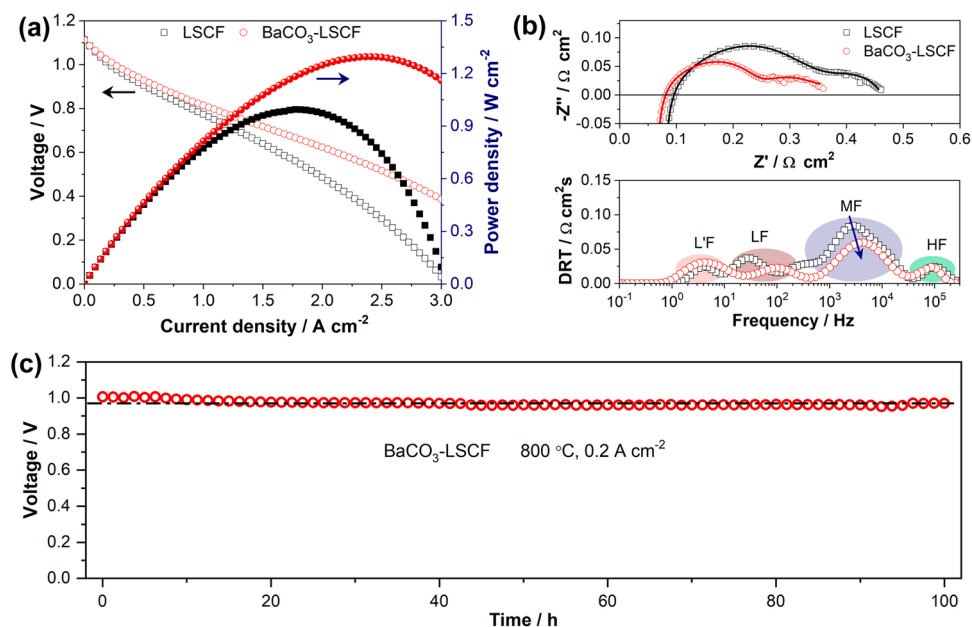


**Fig. 2.** (a) I-V and I-P curves of LSCF and BaCO<sub>3</sub>-LSCF single cells measured at 800 °C. (b) Nyquist plots and DRT analysis of LSCF and BaCO<sub>3</sub>-LSCF cells measured at 800 °C. (c) Galvanostatic stability curve of BaCO<sub>3</sub>-LSCF cell at 800 °C and 0.2 A cm<sup>-2</sup>.

### 3. Results and discussion

#### 3.1. Microstructure and phase

Fig. 1a and b show the SEM images of the surface of as-prepared

LSCF and BaCO<sub>3</sub>-LSCF cathodes. The LSCF cathode is porous and the average particle size is  $274 \pm 105 \text{ nm}$  (Fig. 1a). After the infiltration of  $0.46 \text{ mg cm}^{-2}$  BaCO<sub>3</sub>, there are nanoparticles uniformly distributing on the LSCF cathode (Fig. 1b). The BaCO<sub>3</sub> nanoparticles are in an average size of  $29 \pm 15 \text{ nm}$ . The HRTEM image confirms the distribution of

**Table 1**

Fitted impedance parameters for the LSCF and BaCO<sub>3</sub>-LSCF cells measured at 800 °C.

Samples	LSCF	BaCO <sub>3</sub> -LSCF
$L \times 10^{-6}$ H	1.706	1.341
$R_Q/\Omega \text{ cm}^2$	0.073	0.059
$R_H/\Omega \text{ cm}^2$	0.051	0.049
$Q_H/\times 10^{-3} \text{ F cm}^{-2}$	8.245	10.62
$n_H$	0.987	0.932
$R_M/\Omega \text{ cm}^2$	0.185	0.142
$Q_M/\text{F cm}^{-2}$	0.023	0.037
$n_M$	0.638	0.595
$R_L/\Omega \text{ cm}^2$	0.079	0.071
$Q_L/\text{F cm}^{-2}$	0.559	2.061
$n_L$	0.540	0.654
$R_{L'}/\Omega \text{ cm}^2$	0.075	0.077
$Q_{L'}/\text{F cm}^{-2}$	2.309	17.34
$n_{L'}$	0.719	0.419

orthorhombic BaCO<sub>3</sub> nanoparticles on LSCF with coherent interfaces between the two phases (Fig. 1c). The presence of BaCO<sub>3</sub> on LSCF is also identified by Raman spectroscopy (Fig. 1d) and XRD patterns (Fig. S3a).

### 3.2. Electrochemical performance and stability of single-cells

Fig. 2 shows the  $I$ - $V$  and  $I$ - $P$  curves, impedance spectra, and DRT analysis of the as-prepared single-cells with LSCF and BaCO<sub>3</sub>-LSCF cathodes. It is obvious that the infiltration of BaCO<sub>3</sub> effectively enhances the electrocatalytic activity of the LSCF cathode. The peak power density (PPD) of the LSCF cell is 1.00 W cm<sup>-2</sup> at 800 °C, and increases to 1.30 W cm<sup>-2</sup> for the BaCO<sub>3</sub>-LSCF cell (Fig. 2a). The PPDs of the BaCO<sub>3</sub>-LSCF cell reach 1.16, 0.71, 0.44, and 0.24 W cm<sup>-2</sup> at 750, 700, 650, and 600 °C respectively (Fig. S4a). More importantly, the BaCO<sub>3</sub>-LSCF cell shows excellent operating stability during the galvanostatic test at 800 °C for 100 h (Fig. 2c).

The enhanced electrode activity of LSCF by the infiltration of BaCO<sub>3</sub> is mainly ascribed to the decrease of electrode polarization resistance ( $R_P$ ), as the ohmic resistance ( $R_Q$ ) of LSCF and BaCO<sub>3</sub>-LSCF cells is close at 0.09 and 0.08 Ω cm<sup>2</sup>, respectively.  $R_P$  of the LSCF cell is 0.37 Ω cm<sup>2</sup>, greater than 0.28 Ω cm<sup>2</sup> of the BaCO<sub>3</sub>-LSCF cell (Fig. 2b). The DRT analyses distinguish four peaks at high frequency (HF), medium frequency (MF), low frequency (LF), and extra low frequency (LF') on the impedance spectra. The HF arc is partly related to the oxygen ion transfer from the cathode to the electrolyte, the MF arc is attributed to the adsorption and dissociation of oxygen at the cathode together with the electrochemical process at the anode, and the LF and LF' arcs are connected with the gas diffusion and conversion of the anode substrate [38,53–56]. These assignments are validated by the changes of impedance arcs during varying the temperature and atmospheres at the electrodes (Figs. S4b and S5). An equivalent circuit containing four  $R_i Q_i$  elements ( $i = H, M, L$ , and  $L'$ ) where  $Q$  represents a constant phase element, a  $R_Q$ , and an inductor  $L$  is employed to fit the impedance spectra. The fitted results are tabulated in Table 1. It is observed that the variation between the LSCF and BaCO<sub>3</sub>-LSCF cells mainly lies in the MF arcs (0.18 vs 0.14 Ω cm<sup>2</sup>). As the two cells adopted the identical anodes, the smaller MF arc of BaCO<sub>3</sub>-LSCF cell indicates that the infiltration of BaCO<sub>3</sub> promotes the oxygen adsorption and dissociation on LSCF. Xia et al. also observed that the infiltration of BaCO<sub>3</sub> nanoparticles improves the oxygen surface exchange coefficient of cathodes [57–59]. Zhu et al. reported that the BaO and BaO<sub>2</sub> species segregated on the surface of BSCF are active for the oxygen adsorption/dissociation processes [60]. Chen et al. reported that the infiltration of Ba(NO<sub>3</sub>)<sub>2</sub> into PrBa<sub>0.8</sub>Ca<sub>0.2</sub>Co<sub>2</sub>O<sub>5+δ</sub> (PBCC) cathode resulted in the in situ formation of a highly active BaCoO<sub>3-δ</sub> nanoparticles and thereby enhanced the ORR activity [61].

### 3.3. Cr-tolerance and stability of half-cells

Half-cells were used to evaluate the operating stability of cathodes

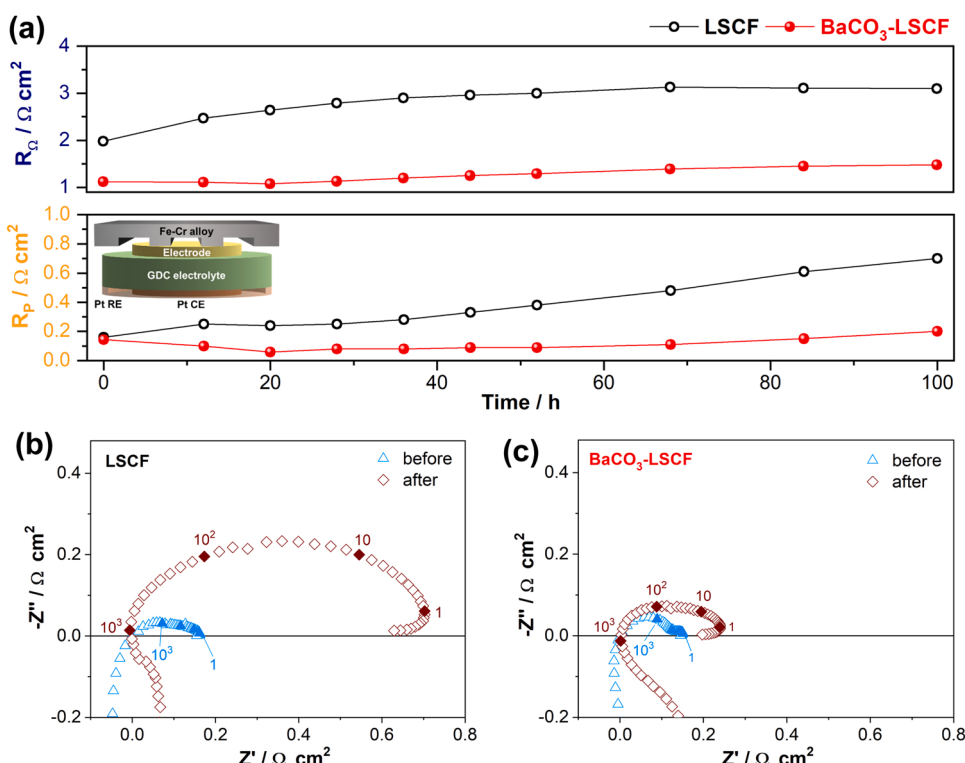
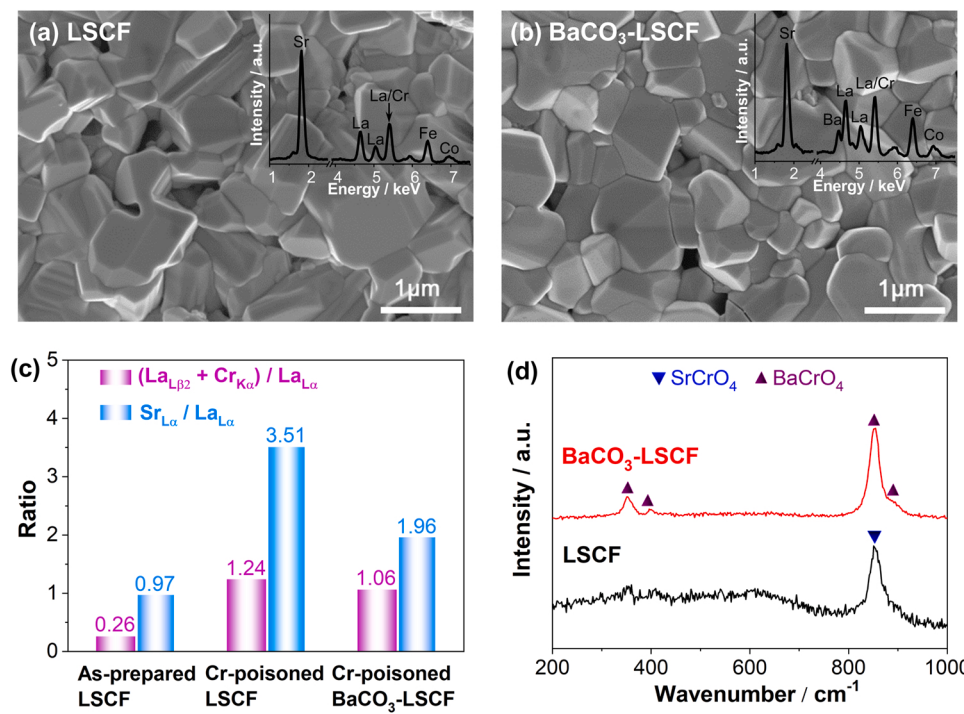
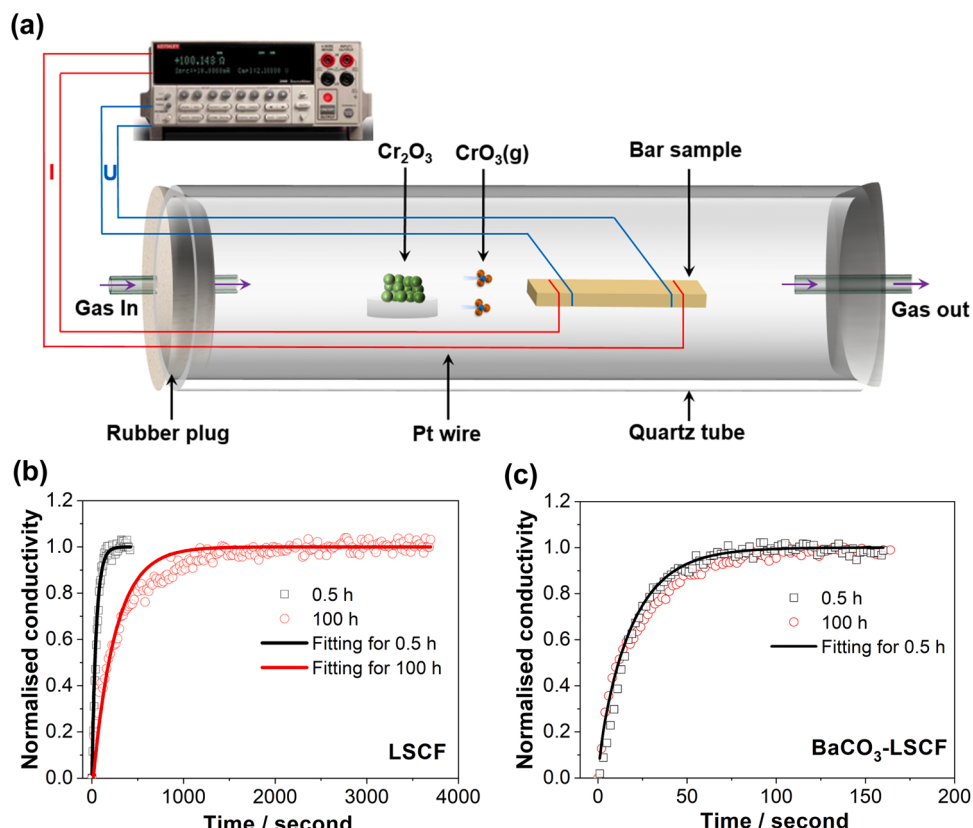


Fig. 3. (a)  $R_Q$  and  $R_P$  plots of LSCF and BaCO<sub>3</sub>-LSCF cathodes during galvanostatic tests at 800 °C and 0.2 A cm<sup>-2</sup> in the presence of Fe-Cr alloy interconnect. Inset is a schematic illustration of half-cells. Nyquist plots of (b) LSCF and (c) BaCO<sub>3</sub>-LSCF cathodes before and after the galvanostatic tests. In (b, c), the high-frequency intercepts are normalized to zero.



under accelerated Cr poisoning conditions. Fig. 3 shows the galvanostatic curves and impedance spectra of LSCF and BaCO<sub>3</sub>-LSCF cathodes in contact with a bare Fe-Cr interconnect at 800 °C. The performance decay of the LSCF cathode indicates the significant Cr poisoning effect,

as is evident by the increase of both  $R_{\Omega}$  and  $R_P$  (Figs. 3a and b). On the contrary, the BaCO<sub>3</sub>-LSCF cathode shows significantly enhanced initial performance and operating stability (Figs. 3a and c), indicating the infiltration of BaCO<sub>3</sub> is very effective in mitigating the deterioration



**Fig. 5.** (a) Schematic illustration of experimental setup for the ECR test under Cr-poisoning conditions. ECR curves as a function of exposure time in the gaseous CrO<sub>3</sub> environment at 800 °C: (b) LSCF and (c) BaCO<sub>3</sub>-LSCF bar samples.

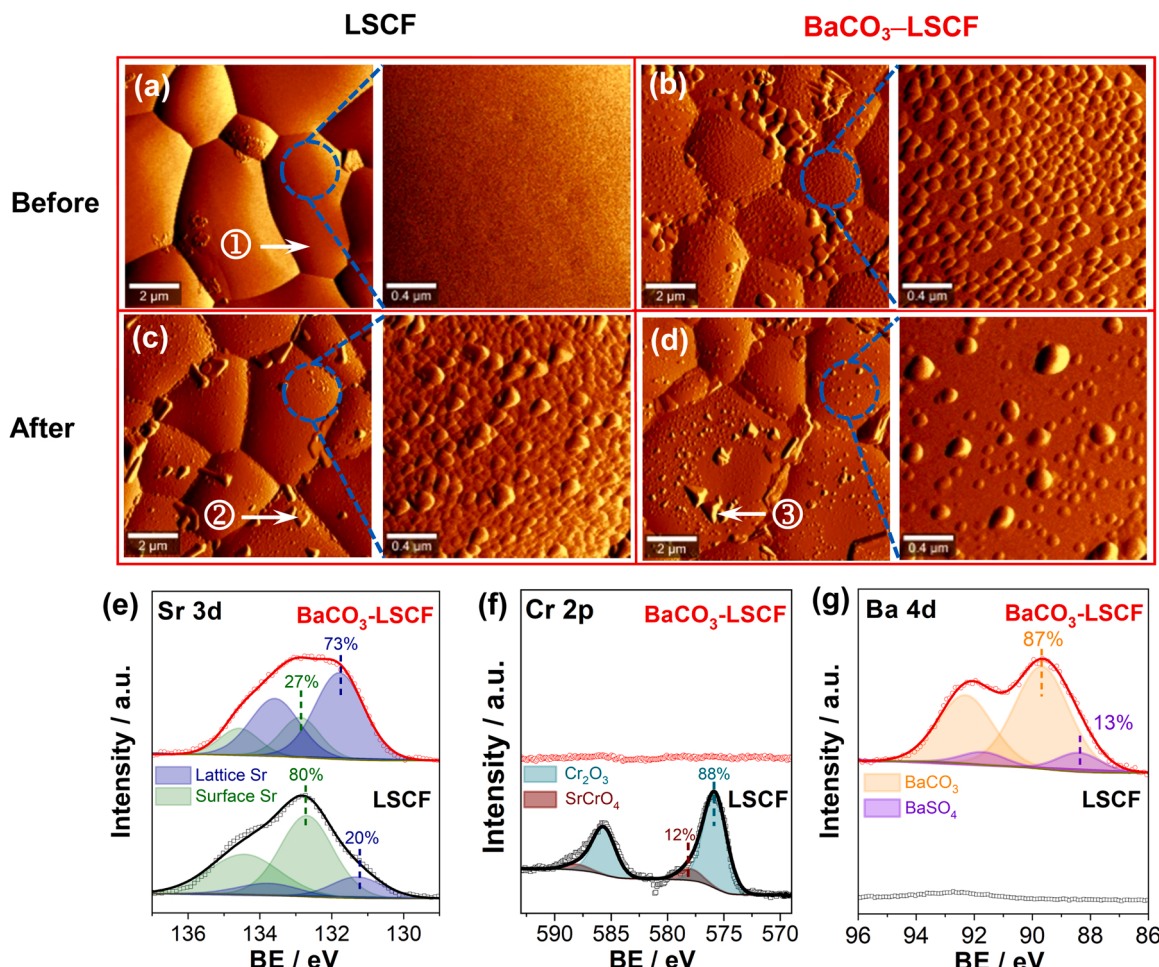


**Fig. 6.** AFM images of as prepared (a) LSCF and (b) BaCO<sub>3</sub>-LSCF bar samples, and tested (c) LSCF and (d) BaCO<sub>3</sub>-LSCF bar samples after exposure in gaseous CrO<sub>3</sub> environment at 800 °C for 100 h. (e) Sr 3d, (f) Cr 2p, and (g) Ba 4d core levels of LSCF and BaCO<sub>3</sub>-LSCF bar samples after exposure in gaseous CrO<sub>3</sub> environment at 800 °C for 100 h. EDS spectra of spots 1–3 are shown in Fig. S8.

effect of chromium poisoning on the LSCF cathodes.

Fig. 4 shows the morphological and elemental analyses of the surface of post-mortem LSCF and BaCO<sub>3</sub>-LSCF cathodes after the Cr poisoning test. The surfaces of both cathodes in contact with the ribs of interconnect become dense, but the morphologies of the grains of the dense layers are different (Figs. 4a and b). According to the elemental and phase analyses, the formation of the dense surface layer of the LSCF cathode is ascribed to the Cr deposition, Sr segregation, and the formation of SrCrO<sub>4</sub> (Figs. 4c, d, and S6). On the other hand, the infiltration of BaCO<sub>3</sub> leads to slightly less Cr deposition and much less Sr segregation on the LSCF cathode (Fig. 4c). Instead of the observation of SrCrO<sub>4</sub> on LSCF, BaCrO<sub>4</sub> was observed on BaCO<sub>3</sub>-LSCF as identified by Raman and XRD analyses (Figs. 4d and S6). Considering the fact that the amount of BaCO<sub>3</sub> is small (0.46 mg cm<sup>-2</sup>, i.e., 3 wt%) and there is certain Sr segregation on the BaCO<sub>3</sub>-LSCF, it is most probable that SrCrO<sub>4</sub> is also formed on the BaCO<sub>3</sub>-LSCF cathode. This is supported by the formation of BaCrO<sub>4</sub> and SrCrO<sub>4</sub> after calcining the BaCO<sub>3</sub>-SrCO<sub>3</sub> mixture together with Cr<sub>2</sub>O<sub>3</sub> at 800 °C (Fig. S7). The detection of only BaCrO<sub>4</sub> signals on BaCO<sub>3</sub>-LSCF is probably attributed to the coverage of SrCrO<sub>4</sub> by BaCrO<sub>4</sub> or the inhibiting effect of BaCrO<sub>4</sub> on the further Sr segregation on LSCF, as is evident by the different morphologies between the dense reaction layers of the two cathodes (Figs. 4a and b).

Under the ribs of interconnect, the solid reaction between the highly active BaCO<sub>3</sub> nanoparticles on the electrode surface and the Cr<sub>2</sub>O<sub>3</sub> scale layer is kinetically fast, and the small amount of BaCO<sub>3</sub> nanoparticles tend to be exhausted shortly. This is supported by the complete reaction

between BaCO<sub>3</sub> and Cr<sub>2</sub>O<sub>3</sub> mixed powders to form BaCrO<sub>4</sub> after calcining at 800 °C for 2 h (Fig. S7). Despite the presence of BaCrO<sub>4</sub> surface layer is useful in mitigating the Cr deposition and Sr surface segregation, the excellent operating stability over the extended duration of test for 100 h implies that there should be other factors contributing to the excellent Cr-tolerance of BaCO<sub>3</sub>-LSCF cathode, as it is possible that the regions of cathodes under the channel of interconnect can be attacked by the gaseous CrO<sub>3</sub> species.

#### 3.4. Cr-tolerance of bar samples

To examine the effect of gaseous CrO<sub>3</sub>, LSCF and BaCO<sub>3</sub>-LSCF bar samples were exposed in gaseous CrO<sub>3</sub> environment at 800 °C (Fig. 5a), and the ECR curves measured during the exposure are shown in Figs. 5b and c. After the exposure in CrO<sub>3</sub> for 0.5 h (time for stabilizing the system), the relaxation time for equilibrium is ~420 s for LSCF (Fig. 5b), longer than that of ~250 s for BaCO<sub>3</sub>-LSCF (Fig. 5c). The fitted surface exchange coefficient ( $K_{chem}$ ) of LSCF is  $9.0 \times 10^{-4} \text{ cm s}^{-1}$ , much smaller than that of  $9.8 \times 10^{-3} \text{ cm s}^{-1}$  for BaCO<sub>3</sub>-LSCF. After the LSCF was exposed in CrO<sub>3</sub> for 100 h, the relaxation time for equilibrium drastically increases to ~3700 s and  $K_{chem}$  decreases sharply to  $1.75 \times 10^{-4} \text{ cm s}^{-1}$ . The drastic decrease in  $K_{chem}$  demonstrates the substantial poisoning effect of gaseous CrO<sub>3</sub> on the surface exchange ability of LSCF. In contrast, the ECR curve of BaCO<sub>3</sub>-LSCF after exposure in CrO<sub>3</sub> for 100 h almost overlaps with that after exposure for 0.5 h, indicating  $K_{chem}$  remains constant regardless of the presence of CrO<sub>3</sub>. This demonstrates

**Table 2**

Summary of binding energies and molar ratios of cations determined by XPS on post-mortem LSCF and BaCO<sub>3</sub>-LSCF bar samples after exposure in gaseous CrO<sub>3</sub> environment at 800 °C for 100 h.

Peaks	Binding energy/eV		Assignment	Ref
	LSCF	BaCO <sub>3</sub> -LSCF		
La 3d <sub>5/2</sub>	833.5	833.1	–	–
	837.4	837.0	–	–
Sr 3d <sub>5/2</sub>	131.3 (20 %)	131.8 (73 %)	Lattice Sr	[63–65]
	132.8 (80 %)	132.9 (27 %)	Surface Sr	[63–65]
Cr 2p <sub>3/2</sub>	575.8 (88 %)	–	Cr <sub>2</sub> O <sub>3</sub>	[66,67]
	578.0 (12 %)	–	SrCrO <sub>4</sub>	[66,67]
Ba 4d <sub>5/2</sub>	–	88.4 (13 %)	BaSO <sub>4</sub>	[68]
	–	89.7 (87 %)	BaCO <sub>3</sub>	[69]
S 2p <sub>3/2</sub>	168.7	169.1	SO <sub>4</sub> <sup>2-</sup>	[62,70]

that the BaCO<sub>3</sub> is very effective in eliminating the detrimental effect of gaseous CrO<sub>3</sub> on LSCF.

Figs. 6a–d show the AFM images of LSCF and BaCO<sub>3</sub>-LSCF bar samples before and after the exposure in CrO<sub>3</sub> at 800 °C for 100 h. For the as-prepared LSCF, the surface is nearly clean and smooth (Fig. 6a). In contrast, on the surface of as-prepared BaCO<sub>3</sub>-LSCF, there are a few agglomerative large particles in the size of 0.63 ± 0.34 μm and many small particles in a size of 121 ± 62 nm with homogenous distribution (Fig. 6b). After the exposure in CrO<sub>3</sub> for 100 h, the surface of post-mortem LSCF becomes very rough due to its coverage with small particles in the size of 137 ± 73 nm (Fig. 6c), and there are also some large particles in the size range of 0.4–2.3 μm (indicated by the arrow, Fig. 6c). The large particles are related to the SrCrO<sub>4</sub> phase as revealed by EDS (Fig. S8). However, on the surface of post-mortem BaCO<sub>3</sub>-LSCF, there are a great number of small grains in the size of 110 ± 70 nm, close to that on the surface of as-prepared sample, and the surface between these particles appears smooth (Fig. 6d). The excellent microstructural stability of the small grains is probably ascribed to the promotional effect of coherent interfaces formed between BaCO<sub>3</sub> and LSCF (Fig. 1c) on suppressing the coarsening of BaCO<sub>3</sub> nanoparticles. In addition, there are also some large deposits in the size of 0.6–2.0 μm (indicated by the arrow, Fig. 6d), with a different shape to the large SrCrO<sub>4</sub> particles on post-mortem LSCF (see Fig. 6c). The EDS results reveal that the large deposits on the BaCO<sub>3</sub>-LSCF consist of distinct Ba and S signals (Figs. S8 and S9). This indicates the existence of BaSO<sub>4</sub>, as is also confirmed by XRD (Fig. S9f). Riedl et al. also reported the observation of sulphate on La<sub>0.6</sub>Sr<sub>0.4</sub>Co<sub>3-δ</sub> (LSC) films due to the presence of a trace amount of sulfur species in the high purity synthetic air [62].

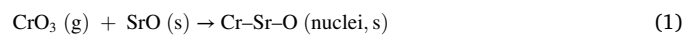
Figs. 6e–g show the XPS core levels on the post-mortem LSCF and BaCO<sub>3</sub>-LSCF bar samples after exposure in gaseous CrO<sub>3</sub> at 800 °C for 100 h, and the binding energies and cation ratios are summarized in Table 2. For the LSCF bar sample, there are lattice and surface Sr cations. The amount of surface Sr of the post-mortem LSCF accounts for as high

as 80 % (Fig. 6e), much higher than 55 % of the as-prepared LSCF (Fig. S3b), indicating significant Sr surface segregation on LSCF. This explains the drastic morphological changes of the post-mortem LSCF bar sample (see Fig. 6c). The deposition of Cr species such as SrCrO<sub>4</sub> and Cr<sub>2</sub>O<sub>3</sub> are also detected (Fig. 6f), implying the interaction of segregated Sr cations with gaseous CrO<sub>3</sub>. The deposition of sulphur in the form of SrSO<sub>4</sub> was also observed (Fig. S10).

For the post-mortem BaCO<sub>3</sub>-LSCF, the percentage of surface Sr is only 27 % (Fig. 6e), which is significantly lower than 80 % of the post-mortem LSCF (Fig. 6e), but close to 29 % of the as-prepared BaCO<sub>3</sub>-LSCF (Fig. S3c). It is worthwhile noting that the percentage of surface oxygen vacancies is close between as-prepared LSCF and BaCO<sub>3</sub>-LSCF bar samples (Fig. S11), and thus the electrostatic interaction between surface oxygen vacancies and lattice Sr cations as the driving force for Sr surface segregation is more or less identical for both the samples [10]. The high stability of surface cations indicates the electrostatic interaction on the BaCO<sub>3</sub>-LSCF bar sample is significantly mitigated by the presence of BaCO<sub>3</sub> nanoparticles. Furthermore, it is interesting that no Cr deposition is observed on BaCO<sub>3</sub>-LSCF (Fig. 6f). These observations indicate that the BaCO<sub>3</sub> nanoparticles effectively eliminate the Sr surface segregation and Cr deposition. In addition, Ba is mainly in the form of BaCO<sub>3</sub> and in a less extent of BaSO<sub>4</sub> (Fig. 6g). According to the time-independent  $K_{\text{chem}}$  values during the long-term ECR tests (Fig. 5c), the deposition of small amount of BaSO<sub>4</sub> phase appears not to deteriorate the oxygen exchange ability of BaCO<sub>3</sub>-LSCF.

### 3.5. Mechanism of Cr-tolerance of BaCO<sub>3</sub> infiltration on LSCF

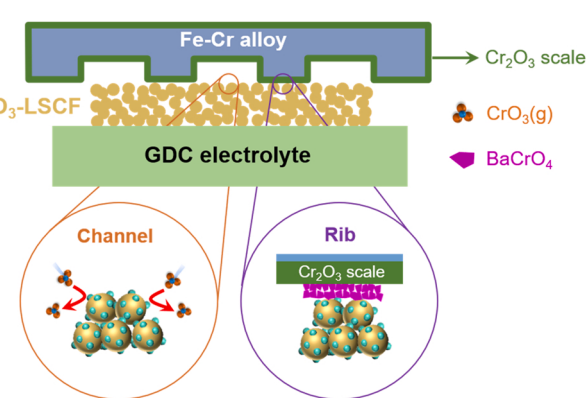
The attack of LSCF cathodes by gaseous CrO<sub>3</sub> has been extensively investigated and the well accepted nucleation theory proposed by Jiang's group can be written as follows.



In this theory, the Cr deposition is initialized by the formation of Sr-Cr-O nuclei due to the interaction between surface segregated SrO and gaseous CrO<sub>3</sub> (Eq. (1)), followed by the crystallization and growth of SrCrO<sub>4</sub> and Cr<sub>2</sub>O<sub>3</sub> grains (Eqs. (2) and (3)). This theory is validated by the significant Sr surface segregation and formation of SrCrO<sub>4</sub> and Cr<sub>2</sub>O<sub>3</sub> on the LSCF bar sample after the exposure in the gaseous CrO<sub>3</sub> environment at 800 °C for 100 h (Figs. 6e and f). Under the accelerated Cr poisoning conditions, severe Cr deposition in the form of SrCrO<sub>4</sub> and Cr<sub>2</sub>O<sub>3</sub> occurs during the solid reaction at the outermost surface of LSCF cathodes. The coverage of LSCF surface by the catalytically inert and electrically insulating SrCrO<sub>4</sub> and Cr<sub>2</sub>O<sub>3</sub> thus increases the ohmic resistance of the LSCF cathodes and deteriorates the oxygen surface exchange ability of the LSCF cathodes and bar samples (Figs. 3a and 5b). The formation of thermodynamically stable SrCrO<sub>4</sub> is the primary driving force to accelerate the Sr surface segregation by the extraction of Sr cations out of the LSCF lattice, leading to the decrease of electrode activity of LSCF (Figs. 3a and b).

The exceptional stability of BaCO<sub>3</sub>-LSCF bar sample in the gaseous CrO<sub>3</sub> environment with no Cr deposition (Fig. 6) is very different to the high tendency of forming BaCrO<sub>4</sub> during the solid-state reaction between BaCO<sub>3</sub> and Cr<sub>2</sub>O<sub>3</sub> (Figs. 4b and S7). This indicates the very low kinetics of the reaction between BaCO<sub>3</sub> nanoparticles and gaseous CrO<sub>3</sub>, in contrast to that of the reaction between the surface segregated Sr species and CrO<sub>3</sub>. This is primarily ascribed to the high reaction energy barrier between BaCO<sub>3</sub> and gaseous CrO<sub>3</sub> [40]. The absence of Cr deposition in the case of BaCO<sub>3</sub>-LSCF bar sample implies that the BaCO<sub>3</sub> nanoparticles are also useful in preventing the deposition of gaseous CrO<sub>3</sub> on the BaCO<sub>3</sub>-LSCF cathode under the channels of interconnect. For the electrode surface in contact with the ribs of interconnect, the

Fig. 7. Schematic diagram of Cr deposition on a BaCO<sub>3</sub>-LSCF cathode.



$\text{BaCO}_3$  nanoparticles rapidly react with the  $\text{Cr}_2\text{O}_3$  scale to form the  $\text{BaCrO}_4$  surface layer, and the reaction can be described by Eq. (4).



The preferential formation of  $\text{BaCrO}_4$  is ascribed to the fact that  $\text{BaCrO}_4$  is more thermodynamically stable than  $\text{SrCrO}_4$  [44,71]. This preferential reaction significantly mitigates the extent of Sr segregation (Fig. 4c) and thereby a much less deteriorating effect on the ohmic resistance and electrode activity of  $\text{BaCO}_3$ -LSCF. The blocking effect of the  $\text{BaCrO}_4$  surface layer has also been reported in the case of BSCF and Ba-doped LSCF cathodes [43,44]. Thus, the blocking effect of  $\text{BaCrO}_4$  surface layer and the very low kinetics of the reaction between  $\text{BaCO}_3$  nanoparticles and gaseous  $\text{CrO}_3$  are responsible for the excellent operating stability of  $\text{BaCO}_3$ -LSCF cathode under the significantly accelerated Cr poisoning conditions, as schematically illustrated in Fig. 7.

#### 4. Conclusions

We have investigated the effects of infiltration of  $\text{BaCO}_3$  nanoparticles on the electrode activity and Cr-tolerance of LSCF materials. The infiltration of  $\text{BaCO}_3$  nanoparticles significantly enhances the oxygen adsorption and dissociation processes of LSCF cathodes and the peak power density increases from  $1.00 \text{ W cm}^{-2}$  for the LSCF cell to  $1.30 \text{ W cm}^{-2}$  for the  $\text{BaCO}_3$ -LSCF cell at  $800^\circ\text{C}$ . The infiltration of  $\text{BaCO}_3$  also dramatically improves the Cr-tolerance of LSCF. After the  $\text{BaCO}_3$ -LSCF bar sample was exposure in the gaseous  $\text{CrO}_3$  environment at  $800^\circ\text{C}$  for 100 h, no Cr deposition and no Sr surface segregation occur, in contrast to the severe Cr deposition and Sr segregation on the LSCF bar samples. The  $\text{BaCO}_3$  nanoparticles retain its original chemical state and morphologies regardless of the presence of gaseous  $\text{CrO}_3$ , demonstrating the very slow kinetics of reaction between  $\text{BaCO}_3$  and  $\text{CrO}_3$  results in the dramatic Cr-tolerance of  $\text{BaCO}_3$ -LSCF. Under the accelerated Cr poisoning conditions using a bare Fe-Cr interconnect, a  $\text{BaCrO}_4$  surface layer is formed on the  $\text{BaCO}_3$ -LSCF cathode and the Sr surface segregation is significantly mitigated. The synergistic effects of the  $\text{BaCrO}_4$  surface layer on mitigating the interaction between segregated Sr cations and Cr species and the very slow chemical kinetics between  $\text{BaCO}_3$  nanoparticles and gaseous  $\text{CrO}_3$  contribute to the remarkable Cr-tolerance and long-term operating stability of LSCF cathode. These findings pave the avenues to the facile fabrication of highly active Cr-tolerant and durable LSCF-based cathodes of IT-SOFCs.

#### CRediT authorship contribution statement

**Jiongyuan Huang:** Data curation, Investigation, Formal analysis, Writing – original draft. **Quan Liu:** Investigation, Data curation. **San Ping Jiang:** Resources, Writing – review & editing. **Ling Zhao:** Investigation, Data curation. **Na Ai:** Methodology, Resources. **Xin Wang:** Investigation, Data curation. **Yanqun Shao:** Formal analysis. **Chengzhi Guan:** Data curation, Resources, Writing – review & editing. **Huihuang Fang:** Investigation, Data curation. **Yu Luo:** Methodology, Resources. **Kongfa Chen:** Supervision, Conceptualization, Writing – review & editing, Funding acquisition.

#### Declaration of Competing Interest

The authors declare that they have no known competing financial interests or personal relationships that could have appeared to influence the work reported in this paper.

#### Data Availability

The authors do not have permission to share data.

#### Acknowledgements

The project was supported by the National Natural Science Foundation of China (22005055, 21875038, and 22279018) and Natural Science Foundation of Fujian Province (2022J01085).

#### Appendix A. Supporting information

Supplementary data associated with this article can be found in the online version at doi:10.1016/j.apcatb.2022.122080.

#### References

- [1] J.H. Zhu, D.A. Chesson, Y.T. Yu, Review— $(\text{Mn},\text{Co})_3\text{O}_4$ -Based Spinels for SOFC interconnect coating application, *J. Electrochem. Soc.* 168 (2021) 114519.
- [2] S.-N. Lee, A. Atkinson, J.A. Kilner, Effect of chromium on  $\text{La}_{0.6}\text{Sr}_{0.4}\text{Co}_{0.2}\text{Fe}_{0.8}\text{O}_{3-\delta}$  solid oxide fuel cell cathodes, *J. Electrochem. Soc.* 160 (2013) F629–F635.
- [3] S.P. Jiang, X. Chen, Chromium deposition and poisoning of cathodes of solid oxide fuel cells – A review, *Int. J. Hydrogen Energy* 39 (2014) 505–531.
- [4] C. Harrison, P. Slater, R. Steinberger-Wilckens, A review of Solid Oxide Fuel Cell cathode materials with respect to their resistance to the effects of chromium poisoning, *Solid State Ion.* 354 (2020), 115410.
- [5] L. Zhou, J.H. Mason, W. Li, X. Liu, Comprehensive review of chromium deposition and poisoning of solid oxide fuel cells (SOFCs) cathode materials, *Renew. Sustain. Energy Rev.* 134 (2020), 110320.
- [6] T. Horita, Chromium poisoning for prolonged lifetime of electrodes in solid oxide fuel cells - review, *Ceram. Int.* 47 (2021) 7293–7306.
- [7] S.P. Jiang, Development of lanthanum strontium cobalt ferrite perovskite electrodes of solid oxide fuel cells - a review, *Int. J. Hydrogen Energy* 44 (2019) 7448–7493.
- [8] J. Ascolani-Yael, A. Montenegro-Hernández, D. Garcés, Q. Liu, H. Wang, K. Yakal-Kremski, S. Barnett, L. Mogni, The oxygen reduction reaction in solid oxide fuel cells: from kinetic parameters measurements to electrode design, *J. Phys.: Energy* 2 (2020), 042004.
- [9] B. Koo, K. Kim, J.K. Kim, H. Kwon, J.W. Han, W. Jung, Sr segregation in perovskite oxides: why it happens and how it exists, *Joule* 2 (2018) 1476–1499.
- [10] K. Chen, S.P. Jiang, Surface segregation in solid oxide cell oxygen electrodes: phenomena, mitigation strategies and electrochemical properties, *Electrochim. Energy Rev.* 3 (2020) 730–765.
- [11] Y. Li, W. Zhang, Y. Zheng, J. Chen, B. Yu, Y. Chen, M. Liu, Controlling cation segregation in perovskite-based electrodes for high electro-catalytic activity and durability, *Chem. Soc. Rev.* 46 (2017) 6345–6378.
- [12] X. Yin, L. Bencze, V. Matalov, R. Spatschek, L. Singheiser, Thermodynamic perspective of Sr-related degradation issues in SOFCs, *Int. J. Appl. Ceram. Technol.* 15 (2018) 380–390.
- [13] J. Druce, H. Téllez, J. Hyodo, Surface segregation and poisoning in materials for low-temperature SOFCs, *MRS Bull.* 39 (2014) 810–815.
- [14] B. Wei, K. Chen, C.C. Wang, Z. Liu, S.P. Jiang, Cr deposition on porous  $\text{La}_{0.6}\text{Sr}_{0.4}\text{Co}_{0.2}\text{Fe}_{0.8}\text{O}_{3-\delta}$  electrodes of solid oxide cells under open circuit condition, *Solid State Ion.* 281 (2015) 29–37.
- [15] S.P. Jiang, S. Zhang, Y.D. Zhen, Deposition of Cr species at  $(\text{La},\text{Sr})(\text{Co},\text{Fe})\text{O}_3$  cathodes of solid oxide fuel cells, *J. Electrochem. Soc.* 153 (2006) A127–A134.
- [16] N. Ni, S.J. Cooper, R. Williams, N. Kemen, D.W. McComb, S.J. Skinner, Degradation of  $(\text{La}_{0.6}\text{Sr}_{0.4})_{0.95}(\text{Co}_{0.2}\text{Fe}_{0.8})\text{O}_{3-\delta}$  solid oxide fuel cell cathodes at the nanometer scale and below, *ACS Appl. Mater. Interfaces* 8 (2016) 17360–17370.
- [17] Y.-L. Huang, A.M. Hussain, C. Pellegrinelli, C. Xiong, E.D. Wachsman, Chromium poisoning effects on surface exchange kinetics of  $\text{La}_{0.6}\text{Sr}_{0.4}\text{Co}_{0.2}\text{Fe}_{0.8}\text{O}_{3-\delta}$ , *ACS Appl. Mater. Interfaces* 9 (2017) 16660–16668.
- [18] L. Zhao, J. Zhang, T. Becker, S.P. Jiang, Raman spectroscopy study of chromium deposition on  $\text{La}_{0.6}\text{Sr}_{0.4}\text{Co}_{0.2}\text{Fe}_{0.8}\text{O}_{3-\delta}$  cathode of solid oxide fuel cells, *J. Electrochem. Soc.* 161 (2014) F687–F693.
- [19] J.A. Schuler, Z. Wuillemin, A. Hessler-Wyser, C. Comminges, N.Y. Steiner, J. Vanherle, Cr-poisoning in  $(\text{La},\text{Sr})(\text{Co},\text{Fe})\text{O}_3$  cathodes after 10,000h SOFC stack testing, *J. Power Sources* 211 (2012) 177–183.
- [20] L. Blum, Q. Fang, S.M. Grob-Barsnick, L.G.J. de Haart, J. Malzbender, N. H. Menzler, W.J. Quadakkers, Long-term operation of solid oxide fuel cells and preliminary findings on accelerated testing, *Int. J. Hydrogen Energy* 45 (2020) 8955–8964.
- [21] L. Zhao, S. Amarasinghe, S.P. Jiang, Enhanced chromium tolerance of  $\text{La}_{0.6}\text{Sr}_{0.4}\text{Co}_{0.2}\text{Fe}_{0.8}\text{O}_{3-\delta}$  electrode of solid oxide fuel cells by  $\text{Gd}_{0.1}\text{Ce}_{0.9}\text{O}_{1.95}$  impregnation, *Electrochim. Commun.* 37 (2013) 84–87.
- [22] D.R. Ou, M. Cheng, Stability of manganese-oxide-modified lanthanum strontium cobaltite in the presence of chromia, *J. Power Sources* 272 (2014) 513–517.
- [23] J. Li, J. Li, D. Yan, J. Pu, B. Chi, L. Jian, Promoted Cr-poisoning tolerance of  $\text{La}_2\text{NiO}_{4+\delta}$ -coated  $\text{PrBa}_{0.5}\text{Sr}_{0.5}\text{Co}_{1.5}\text{Fe}_{0.5}\text{O}_{5+\delta}$  cathode for intermediate temperature solid oxide fuel cells, *Electrochim. Acta* 270 (2018) 294–301.
- [24] P. Qiu, J. Li, L. Jia, B. Chi, J. Pu, J. Li, F. Chen,  $\text{LaCoO}_{3-\delta}$  coated  $\text{Ba}_{0.5}\text{Sr}_{0.5}\text{Co}_{0.8}\text{Fe}_{0.2}\text{O}_{3-\delta}$  cathode for intermediate temperature solid oxide fuel cells, *Electrochim. Acta* 319 (2019) 981–989.
- [25] X.Y. Zhao, Y.F. Yan, M.Z. Li, X.F. Ding, In-situ strategy to suppress chromium poisoning on  $\text{La}_{0.6}\text{Sr}_{0.4}\text{Co}_{0.2}\text{Fe}_{0.8}\text{O}_{3-\delta}$  cathodes of solid oxide fuel cells, *Int. J. Hydrogen Energy* 44 (2019) 30401–30408.

- [26] T. Yang, Y. Wen, T. Wu, N. Xu, K. Huang, A highly active and Cr-resistant infiltrated cathode for practical solid oxide fuel cells, *J. Mater. Chem. A* 8 (2020) 82–86.
- [27] H. Zhang, K. Xu, F. He, Y. Zhou, K. Sasaki, B. Zhao, Y. Choi, M. Liu, Y. Chen, Surface regulating of a double-perovskite electrode for protonic ceramic fuel cells to enhance oxygen reduction activity and contaminants poisoning tolerance, *Adv. Energy Mater.* 12 (2022) 2200761.
- [28] J. Hong, A.N. Aphale, S.J. Heo, B. Hu, M. Reisert, S. Belko, P. Singh, Strontium manganese oxide getter for capturing airborne Cr and S contaminants in high-temperature electrochemical systems, *ACS Appl. Mater. Interfaces* 11 (2019) 34878–34888.
- [29] Z. Wang, S. Zhao, X. Guo, J. Li, Q. Hu, Y. Feng, F. Yu, H. Sun, Inhibition of chromium poisoning in  $\text{La}_{0.6}\text{Sr}_{0.4}\text{Co}_{0.2}\text{Fe}_{0.8}\text{O}_{3-\delta}$  cathode via simple electroless silver plating for solid oxide fuel cells, *Int. J. Hydrogen Energy* 47 (2022) 11250–11260.
- [30] Y. Zhen, S.P. Jiang, Characterization and performance of  $(\text{La}, \text{Ba})(\text{Co}, \text{Fe})\text{O}_3$  cathode for solid oxide fuel cells with iron-chromium metallic interconnect, *J. Power Sources* 180 (2008) 695–703.
- [31] X.B. Chen, L. Zhang, S.P. Jiang, Chromium deposition and poisoning on  $(\text{La}_{0.8}\text{Sr}_{0.4-x}\text{Ba}_x)(\text{Co}_{0.2}\text{Fe}_{0.8})\text{O}_3$  ( $0 \leq x \leq 0.4$ ) cathodes of solid oxide fuel cells, *J. Electrochem. Soc.* 155 (2008) B1093–B1101.
- [32] Y.M. Kim, X.B. Chen, S.P. Jiang, J. Bae, Chromium deposition and poisoning at  $\text{Ba}_{0.5}\text{Sr}_{0.5}\text{Co}_{0.8}\text{Fe}_{0.2}\text{O}_{3-\delta}$  cathode of solid oxide fuel cells, *Electrochim. Solid State Lett.* 14 (2011) B41–B45.
- [33] Y.M. Kim, X.B. Chen, S.P. Jiang, J. Bae, Effect of strontium content on chromium deposition and poisoning in  $\text{Ba}_{1-x}\text{Sr}_x\text{Co}_{0.8}\text{Fe}_{0.2}\text{O}_{3-\delta}$  ( $0.3 \leq x \leq 0.7$ ) cathodes of solid oxide fuel cells, *J. Electrochim. Soc.* 159 (2012) B185–B194.
- [34] L. Zhao, Y. Cheng, S.P. Jiang, A new, high electrochemical activity and chromium tolerant cathode for solid oxide fuel cells, *Int. J. Hydrogen Energy* 40 (2015) 15622–15631.
- [35] J. Wang, Z. Yang, K. Yang, Y. Chen, X. Xiong, S. Peng, Chromium deposition and poisoning on  $\text{Ba}_{0.9}\text{Co}_{0.2}\text{Fe}_{0.2}\text{Nb}_{0.1}\text{O}_{3-\delta}$  cathode of solid oxide fuel cells, *Electrochim. Acta* 289 (2018) 503–515.
- [36] Z. Li, B. Guan, F. Xia, J. Nie, W. Li, L. Ma, W. Li, L. Zhou, Y. Wang, H. Tian, J. Luo, Y. Chen, M. Frost, K. An, X. Liu, High entropy perovskite as high performing chromium-tolerant cathode for solid oxide fuel cells, *ACS Appl. Mater. Interfaces* 14 (2022) 24363–24373.
- [37] X.B. Chen, S.P. Jiang, Highly active and stable  $(\text{La}_{0.24}\text{Sr}_{0.16}\text{Ba}_{0.6})(\text{Co}_{0.5}\text{Fe}_{0.44}\text{Nb}_{0.06})\text{O}_{3-\delta}$  (LSBCFN) cathodes for solid oxide fuel cells prepared by a novel mixing synthesis method, *J. Mater. Chem. A* 1 (2013) 4871–4878.
- [38] Y. Chen, Y. Choi, S. Yoo, Y. Ding, R. Yan, K. Pei, C. Qu, L. Zhang, I. Chang, B. Zhao, Y. Zhang, H. Chen, Y. Chen, C. Yang, B. deGlee, R. Murphy, J. Liu, M. Liu, A highly efficient multi-phase catalyst dramatically enhances the rate of oxygen reduction, *Joule* 2 (2018) 938–949.
- [39] K. Pei, Y. Zhou, K. Xu, Z. He, Y. Chen, W. Zhang, S. Yoo, B. Zhao, W. Yuan, M. Liu, Y. Chen, Enhanced Cr-tolerance of an SOFC cathode by an efficient electro-catalyst coating, *Nano Energy* 72 (2020), 104704.
- [40] Y. Niu, Y. Zhou, W. Lv, Y. Chen, Y. Zhang, W. Zhang, Z. Luo, N. Kane, Y. Ding, L. Soule, Y. Liu, W. He, M. Liu, Enhancing oxygen reduction activity and Cr tolerance of solid oxide fuel cell cathodes by a multiphase catalyst coating, *Adv. Funct. Mater.* 31 (2021) 2100034.
- [41] J. Huang, Z. Xie, N. Ai, C.C. Wang, S.P. Jiang, X. Wang, Y. Shao, K. Chen, A hybrid catalyst coating for a high-performance and chromium-resistive cathode of solid oxide fuel cells, *Chem. Eng. J.* 431 (2022), 134281.
- [42] K. Chen, N. Ai, K.M. O'Donnell, S.P. Jiang, Highly chromium contaminant tolerant BaO infiltrated  $\text{La}_{0.6}\text{Sr}_{0.4}\text{Co}_{0.2}\text{Fe}_{0.8}\text{O}_{3-\delta}$  cathodes for solid oxide fuel cells, *Phys. Chem. Chem. Phys.* 17 (2015) 4870–4874.
- [43] F. Shen, K. Lu, Perovskite-type  $\text{La}_{0.6}\text{Sr}_{0.4}\text{Co}_{0.2}\text{Fe}_{0.8}\text{O}_3$ ,  $\text{Ba}_{0.5}\text{Sr}_{0.5}\text{Co}_{0.2}\text{Fe}_{0.8}\text{O}_3$ , and  $\text{Sm}_{0.5}\text{Sr}_{0.5}\text{Co}_{0.2}\text{Fe}_{0.8}\text{O}_3$  cathode materials and their chromium poisoning for solid oxide fuel cells, *Electrochim. Acta* 211 (2016) 445–452.
- [44] M. Xie, C. Cai, X. Liu, K. Xue, Y. Chen, J. Peng, J. Bao, S. An, H. Yang, Improved durability of high-performance intermediate-temperature solid oxide fuel cells with a Ba-doped  $\text{La}_{0.6}\text{Sr}_{0.4}\text{Co}_{0.2}\text{Fe}_{0.8}\text{O}_{3-\delta}$  cathode, *ACS Appl. Mater. Interfaces* 14 (2022) 33052–33063.
- [45] Z. Chen, W. Jiang, Z. Lu, Z. Wang, Z. Chen, S.P. Jiang, T. Lin, Y. Shao, D. Tang, K. Chen, N. Ai, Accelerating effect of polarization on electrode/electrolyte interface generation and electrocatalytic performance of  $\text{Er}_{0.4}\text{Bi}_{1.6}\text{O}_3$  decorated  $\text{Sm}_{0.95}\text{CoO}_{3-\delta}$  cathodes, *J. Power Sources* 465 (2020), 228281.
- [46] Z. Yue, L. Jiang, N. Ai, C. Guan, S.P. Jiang, X. Sun, W.D.A. Rickard, X. Wang, Y. Shao, K. Chen, Facile co-synthesis and utilization of ultrafine and highly active  $\text{PrBa}_{0.8}\text{Ca}_{0.2}\text{Co}_{2}\text{O}_{5+\delta}\text{-Gd}_{0.2}\text{Ce}_{0.8}\text{O}_{1.9}$  composite cathodes for solid oxide fuel cells, *Electrochim. Acta* 403 (2022), 139673.
- [47] Y. Zou, T. Lin, Y. Sun, Z. Chen, C. Guan, Y. Li, S.P. Jiang, N. Ai, K. Chen, Anodic polarization creates an electrocatalytically active Ni anode/electrolyte interface and mitigates the coarsening of Ni phase in SOFC, *Electrochim. Acta* 391 (2021), 138912.
- [48] F. Ciucci, C. Chen, Analysis of electrochemical impedance spectroscopy data using the distribution of relaxation times: a bayesian and hierarchical bayesian approach, *Electrochim. Acta* 167 (2015) 439–454.
- [49] M.B. Effat, F. Ciucci, Bayesian and hierarchical bayesian based regularization for deconvolving the distribution of relaxation times from electrochemical impedance spectroscopy data, *Electrochim. Acta* 247 (2017) 1117–1129.
- [50] T. Horita, Y. Xiong, M. Yoshinag, H. Kishimoto, K. Yamaji, M.E. Brito, H. Yokokawa, Determination of chromium concentration in solid oxide fuel cell cathodes:  $(\text{La}, \text{Sr})\text{MnO}_3$  and  $(\text{La}, \text{Sr})\text{FeO}_3$ , *Electrochim. Solid-State Lett.* 12 (2009) B146–B149.
- [51] B.B. Ebbinghaus, Thermodynamics of gas phase chromium species: The chromium oxides, the chromium oxyhydroxides, and volatility calculations in waste incineration processes, *Cambust. Flame* 93 (1993) 119–137.
- [52] L. Zhao, J. Hyodo, K. Chen, N. Ai, S. Amarasinghe, T. Ishihara, S. Ping Jiang, Effect of boron deposition and poisoning on the surface exchange properties of lscf electrode materials of solid oxide fuel cells, *J. Electrochim. Soc.* 160 (2013) F682–F686.
- [53] M. Ghamarinia, A. Babaei, C. Zamani, Electrochemical characterization of  $\text{La}_2\text{NiO}_4$ -infiltrated  $\text{La}_{0.6}\text{Sr}_{0.4}\text{Co}_{0.2}\text{Fe}_{0.8}\text{O}_{3-\delta}$  by analysis of distribution of relaxation times, *Electrochim. Acta* 353 (2020), 136520.
- [54] Y. Namgung, J. Hong, A. Kumar, D.-K. Lim, S.-J. Song, One step infiltration induced multi-cation oxide nanocatalyst for load proof SOFC application, *Appl. Catal. B: Environ.* 267 (2020), 118374.
- [55] Y. Chen, S. Yoo, Y. Choi, J.H. Kim, Y. Ding, K. Pei, R. Murphy, Y. Zhang, B. Zhao, W. Zhang, H. Chen, Y. Chen, W. Yuan, C. Yang, M. Liu, A highly active,  $\text{CO}_2$ -tolerant electrode for the oxygen reduction reaction, *Energy Environ. Sci.* 11 (2018) 2458–2466.
- [56] Z. Chen, L. Jiang, S. He, C. Guan, Y. Zou, Z. Yue, N. Ai, S.P. Jiang, Y. Shao, K. Chen, Development of intertwined nanostructured multi-phase air electrodes for efficient and durable reversible solid oxide cells, *Appl. Catal. B: Environ.* 305 (2022), 121056.
- [57] T. Hong, F. Chen, C. Xia, Barium carbonate nanoparticle as high temperature oxygen reduction catalyst for solid oxide fuel cell, *Electrochim. Commun.* 51 (2015) 93–97.
- [58] T. Hong, K.S. Brinkman, C. Xia, Barium carbonate nanoparticles as synergistic catalysts for the oxygen reduction reaction on  $\text{La}_{0.6}\text{Sr}_{0.4}\text{Co}_{0.2}\text{Fe}_{0.8}\text{O}_{3-\delta}$  solid-oxide fuel cell cathodes, *ChemElectroChem* 3 (2016) 805–813.
- [59] T. Hong, F. Chen, C. Xia, Barium carbonate nanoparticle to enhance oxygen reduction activity of strontium doped lanthanum ferrite for solid oxide fuel cell, *J. Power Sources* 278 (2015) 741–750.
- [60] Y. Zhu, D. Liu, H. Jing, F. Zhang, X. Zhang, S. Hu, L. Zhang, J. Wang, L. Zhang, W. Zhang, B. Pang, P. Zhang, F. Fan, J. Xiao, W. Liu, X. Zhu, W. Yang, Oxygen activation on Ba-containing perovskite materials, *Sci. Adv.* 8 (2022) 4072.
- [61] Y. Chen, S. Yoo, W. Zhang, Y. Zhang, J.H. Kim, Y. Zhou, K. Pei, N. Kane, B. Zhao, R. Murphy, Y. Choi, M. Liu, Effective promotion of oxygen reduction reaction by in situ formation of nanostructured catalyst, *ACS Catal.* 9 (2019) 7137–7142.
- [62] C. Riedl, M. Siebenhofer, A. Nenning, A. Schmid, M. Weiss, C. Rameshan, A. Limbeck, M. Kubicek, A.K. Opitz, J. Fleig, In situ techniques reveal the true capabilities of SOFC cathode materials and their sudden degradation due to omnipresent sulfur trace impurities, *J. Mater. Chem. A* 10 (2022) 14838–14848.
- [63] D. Tripković, J. Wang, R. Küngas, M.B. Mogensen, B. Yıldız, P.V. Hendriksen, Thermally controlled activation and passivation of surface chemistry and oxygen-exchange kinetics on a perovskite oxide, *Chem. Mater.* 34 (2022) 1722–1736.
- [64] N. Ai, S. He, N. Li, Q. Zhang, W.D.A. Rickard, K. Chen, T. Zhang, S.P. Jiang, Suppressed Sr segregation and performance of directly assembled  $\text{La}_{0.6}\text{Sr}_{0.4}\text{Co}_{0.2}\text{Fe}_{0.8}\text{O}_{3-\delta}$  oxygen electrode on  $\text{Y}_{2}\text{O}_{3}\text{-ZrO}_2$  electrolyte of solid oxide electrolysis cells, *J. Power Sources* 384 (2018) 125–135.
- [65] M.R. Ardigo, A. Perron, L. Combemale, O. Heintz, G. Caboche, S. Chevalier, Interface reactivity study between  $\text{La}_{0.6}\text{Sr}_{0.4}\text{Co}_{0.2}\text{Fe}_{0.8}\text{O}_{3-\delta}$  (LSCF) cathode material and metallic interconnect for fuel cell, *J. Power Sources* 196 (2011) 2037–2045.
- [66] D. Chen, B. Mewafa, F. Paloukis, L. Zhong, V. Papaefthimiou, T. Dintzer, K. M. Papazisi, S.P. Balomenou, D. Tsiplikides, D. Teschner, V. Pérez-Dieste, C. Escudero, S. Zafeiratos, Revising the role of chromium on the surface of perovskite electrodes: Poison or promoter for the solid oxide electrolysis cell performance? *J. Catal.* 381 (2020) 520–529.
- [67] D. Chidambaram, Gary P. Halada, C.R. Clayton, Development of a technique to prevent radiation damage of chromate conversion coatings during X-ray photoelectron spectroscopic analysis, *Appl. Surf. Sci.* 181 (2001) 283–295.
- [68] F. Bozheyev, F. Xi, I. Ahmed, C. Höhn, K. Ellmer, Evaluation of Pt, Rh,  $\text{SnO}_2$ ,  $(\text{NH}_4)_2\text{Mo}_3\text{S}_13$ ,  $\text{BaSO}_4$  protection coatings on  $\text{WSe}_2$  photocathodes for solar hydrogen evolution, *Int. J. Hydrogen Energy* 45 (2020) 19112–19120.
- [69] J.-I. Jung, D.D. Edwards, X-ray photoelectron (XPS) and Diffuse Reflectance Infra Fourier Transformation (DRIFT) study of  $\text{Ba}_{0.5}\text{Sr}_{0.5}\text{Co}_x\text{Fe}_{1-x}\text{O}_{3-\delta}$  (BSCF:  $x=0\text{-}0.8$ ) ceramics, *J. Solid State Chem.* 184 (2011) 2238–2243.
- [70] C.C. Wang, K. O'Donnell, L. Jian, S.P. Jiang, Co-deposition and poisoning of chromium and sulfur contaminants on  $\text{La}_{0.6}\text{Sr}_{0.4}\text{Co}_{0.2}\text{Fe}_{0.8}\text{O}_{3-\delta}$  cathodes of solid oxide fuel cells, *J. Electrochim. Soc.* 162 (2015) F507–F512.
- [71] N. Sakai, T. Horita, K. Yamaji, Y.P. Xiong, H. Kishimoto, M.E. Brito, H. Yokokawa, Material transport and degradation behavior of SOFC interconnects, *Solid State Ion.* 177 (2006) 1933–1939.